Astronomy & Astrophysics manuscript no. PSP_near_fce_burst_draft_v09_integrated_changes_2column
April 3, 2021

Electron Bernstein waves and narrow band plasma waves near the electron cyclotron frequency in the near-Sun solar wind

D. M. Malaspina[1,2], L.B. Wilson III[3], R. E. Ergun[1,2], S.D. Bale[4,5], J.W.Bonnell[4], K. Goodrich[4], K. Goetz[6], P.R. Harvey[4], R.J. MacDowall[3], M. Pulupa[4], J. Halekas[7], A. Case[8], J.C. Kasper[9], D. Larson[4], M. Stevens[8], and P. Whittlesey[4]

[1] Laboratory for Atmospheric and Space Physics, University of Colorado, Boulder, CO, USA,
e-mail: David.Malaspina@lasp.colorado.edu
[2] Astrophysical and Planetary Sciences Department, University of Colorado, Boulder, CO, USA,
[3] NASA Goddard Spaceflight Center, Greenbelt, MD, USA

[4] Space Sciences Laboratory, University of California, Berkeley, CA, USA

[5] Physics Department, University of California, Berkeley, CA, USA

[6] School of Physics and Astronomy, University of Minnesota, Minneapolis, MN, USA

[7] Department of Physics and Astronomy, University of Iowa, Iowa City, Iowa, USA

[8] Harvard-Smithsonian Center for Astrophysics, Cambridge, MA, USA

[9] University of Michigan, Ann Arbor, MI, USA

Received ... 2021; accepted ... 2021

ABSTRACT

Context. Recent studies of the solar wind sunward of 0.25 AU reveal that it contains quiescent regions, with low amplitude plasma and magnetic field fluctuations and Parker-spiral like magnetic field direction. The quiescent regions are thought to have more direct magnetic connection to the solar corona compared with other types of solar wind, suggesting that waves or instabilities in the quiescent regions are indicative of the early evolution of the solar wind as it escapes the corona. The quiescent solar wind regions are highly unstable to the formation of plasma waves near the electron cyclotron frequency (f_{ce}).
Aims. In this study, we examine high time resolution observations of these waves in an effort to understand their impact on electron distribution functions of the quiescent near-Sun solar wind.
Methods. High time resolution waveform captures of near-f_{ce} waves are examined to determine variations of their amplitude and frequency in time as well as their polarization properties.
Results. We demonstrate that the near-f_{ce} wave intervals contain several distinct wave types, including electron Bernstein waves and extremely narrow band waves that are highly sensitive to the ambient magnetic field orientation. Using properties of these waves, we suggest possible plasma wave mode classifications, and possible instabilities responsible for generating these waves. The results of this analysis indicate that these waves act to modify the cold core of the electron distribution functions in the quiescent near-Sun solar wind.

Key words. plasma waves – solar wind – wave-particle interactions

1. Introduction

Recent studies have demonstrated that solar wind particle distributions are highly unstable to the growth of plasma waves at distances from the Sun smaller than ∼ 55 solar radii (∼0.25 astronomical units). Plasma wave modes reported in this region of space include narrowband waves such as ion cyclotron waves (Bowen et al. 2020; Verniero et al. 2020), whistler-mode waves (Agapitov et al. 2020; Jagarlamudi et al. 2020; Cattell et al. 2021), Langmuir waves (Bale et al. 2019), ion acoustic waves (Mozer2020, Kromyda et al. 2021, submitted), and waves near the electron cyclotron frequency (Malaspina et al. 2020). Broadband waves have also been reported, including kinetic Alfvén waves (Chaston et al. 2020) and plasma turbulent fluctuations (Chen et al. 2020; Zhao et al. 2020; Zhu et al. 2020).

Plasma waves are important to the system-scale dynamics of the solar wind because they act to transfer energy from one part of solar wind particle distributions, the wave unstable region, to other parts of the distribution where wave damping occurs. In this way, energy exchange mediated by plasma waves homogenizes mixed plasmas, smooths discontinuous distributions, relaxes particle beam distributions, and scatters particles in pitch angle.

This study focuses on plasma waves near the electron cyclotron frequency (f_{ce}) in the near-Sun solar wind. These waves, as reported in Malaspina et al. (2020), were found to preferentially occur in regions of extraordinarily low amplitude magnetic

fluctuations (quiescent solar wind regions), where the solar wind magnetic field vector (**B**) remains within ~ 5^o of the theoretical Parker spiral direction. Additionally, the quiescent solar wind regions show distinctly different spectra of turbulent fluctuations, with 50 times higher frequency of the $1/f$ spectral break location compared to regions of the solar wind with switchbacks, consistent with less evolved solar wind in the quiescent regions (Dudok de Wit et al. 2020). Regions of high wave growth were found to coincide with strong sunward drift of the electron core population, suggesting that the coincident electron strahl population was denser, focused more narrowly into a beam, or extended to higher energy compared to surrounding regions. These properties: low amplitude ambient magnetic field fluctuations, Parker-spiral **B** vector, higher $1/f$ spectral break frequency, and strong sunward electron core drift, are consistent with the interpretation that these regions of high wave growth represent portions of the solar wind most directly magnetically connected to the solar corona. As such, these near-f_{ce} waves may play an important role in the evolution of solar wind electrons early in their escape from the solar corona.

These near-f_{ce} waves were found to have two primary wave power peaks, one near f_{ce} and one near $0.7f_{ce}$, and many higher harmonics of both frequencies. The waves were found to persist for time periods ranging from minutes to many hours. They were found to increase in occurrence and amplitude with decreasing distance to the Sun. The wave mode was not conclusively identified in Malaspina et al. (2020), though it was speculated that they might be electrostatic whistler-mode or electron Bernstein waves. In this analysis, properties of studied near-f_{ce} waves are found to be inconsistent with prior observations of whistler-mode waves in the solar wind (e.g. (Zhang et al. 1998; Lacombe et al. 2014; Stansby et al. 2016; Tong et al. 2019))

Malaspina et al. (2020) used relatively low cadence (~ 0.87s), highly compressed survey spectral data from the Parker Solar Probe spacecraft to examine these waves. In the current study, the detailed properties of these waves are examined using 'burst' captures of high-cadence time series electric and magnetic field data. These data enable a wealth of new wave properties to be determined, narrowing the list of possible wave modes, and offering new understanding of the instabilities that drive these waves, as well as elucidating the impact that they have on the evolution of solar wind electron distribution functions.

The findings are surprising, demonstrating that: (i) the near-f_{ce} waves consist of at least three separate but simultaneously occurring wave modes, one of which can be conclusively identified as electron Bernstein waves and (ii) the portion of the electron distribution function unstable to wave growth is at exceptionally low energies, near the center of the electron core distribution. Further, the data examined here constrain the wave polarization, wave vector direction and magnitude, and suggest a possible geometry for the wave source regions.

2. Data

This analysis uses data from the Parker Solar Probe mission (Fox et al. 2016), primarily the FIELDS (Bale et al. 2016) and SWEAP (Kasper et al. 2016) instruments. The full Parker Solar Probe mission consists of 24 orbits of the Sun. Each close approach to the Sun (<55 solar radii (R_S)) is referred to as an encounter, and sequentially numbered. At the time of writing, 7 encounters have been completed.

This study uses data from the four FIELDS voltage sensors in the plane of the heat shield, operated as differential pairs (V_{12}, V_{34}), as well as magnetic field data from the Fluxgate Magnetometer (FGM) and Search Coil Magnetometer (SCM). Both survey and burst data products from the Digital Fields Board (DFB) (Malaspina et al. 2016) are also used, including the AC-coupled survey power spectra (covering ~140 Hz to 75 kHz at a cadence of ~0.87 s) and triggered time series bursts (150 kS/s for ~3.5 s). Quasi-thermal noise measurements from the Radio Frequency Spectrometer (RFS) (Pulupa et al. 2017), at a cadence of 16 s, are used to determine electron plasma density. This study uses data from SWEAP, primarily proton velocity as determined by the Faraday cup (Case et al. 2020).

FIELDS and SWEAP data are presented in the spacecraft coordinate system (and the spacecraft reference frame), where $+\hat{z}$ points Sunward, $+\hat{x}$ points in the direction of motion of the spacecraft about the Sun (ram), and $+\hat{y}$ completes the orthogonal set, pointing approximately ecliptic south. To derive electric field amplitudes, the differential pair voltage data (V_{12}, V_{34}) are rotated into spacecraft coordinates and divided by an effective electrical length of 3.5 m (Mozer et al. 2020).

This study contains an analysis of one time series burst, recorded near June 6, 2020, 12:09:54 UTC (encounter 5), but the results are generally applicable to similar bursts captured during any of the encounters examined thus far. Several hundred bursts of this type (150 kS/s for ~3.5 s, six channels of time series data) are captured per solar encounter. These bursts are selected via an on-board algorithm which seeks the highest amplitude signals in V_{12} time-series data. During each of the first seven encounters, several tens of these bursts contain waves of the type explored here. The waves under study are frequently observed in the continuously recorded survey data (Malaspina et al. 2020).

3. Burst Data Analysis

Figure 1 shows the solar wind conditions for two minutes before and after the time-series burst of interest, which begins near June 6, 2020, 12:09:54 UTC. Figure 1a shows survey power spectra from ~200 Hz to 75 kHz, with spectra produced once per ~0.87 s. The power shown is the summed power from the two differential pair signals (V_{12} + V_{34}). The electron cyclotron frequency (f_{ce}) is indicated by a white dashed line, and the time of burst capture is indicated by vertical black dashed lines. Figure 1b shows measurements from the FGM (sampled at ~ 293 sample/s). Figure 1c shows the proton velocity vector as determined by SWEAP Faraday Cup, and Figure 1d shows the plasma density as determined by quasi thermal noise fitting (Moncuquet et al. 2020). The velocities shown are in the frame of the spacecraft. Figure 1e shows the time-series waveforms under study (black = E_x, blue = E_y), sampled at 150,000 samples/s.

Key features of the near-f_{ce} waves described in Malaspina et al. (2020) are observed, including steady wave power near 0.7 f_{ce} and f_{ce}, and extensive harmonic structure. The background magnetic field points close to the nominal Parker spiral direction for this radial distance from the Sun (~28.85 R_S). The fluctuation amplitude of the magnetic field is low, such that $(< \delta B > / < |B| >) \approx 6.3\times10^{-2}$, where $\delta B = \sqrt{\delta B_x^2 + \delta B_y^2 + \delta B_z^2}$ and $\delta B_x = B_x - < B_x >$, and all averages are taken over the ~ 200 s interval shown in Figure 1b. The solar wind flow velocity is ~250 km/s in the frame of the spacecraft and the density is ~600 cm^{-3}. One significant difference from the observations reported in Malaspina et al. (2020) is that near-f_{ce} waves observed closer to the Sun than ~35 R_S (close approaches of encounters 4,5,6) often show broadband bursts of wave power in addition to

prominent lines near ~0.7 f_{ce} and ~1.0 f_{ce}. The prominent lines become strong during the broadband bursts.

During this interval, the Debye length (λ_D) is ~ 1.9 m, the electron gyro radius is ~97 m, $|B| \approx$ 152nT, $T_e \approx$ 38 eV, and the electron thermal speed is ~3,700 km/s. The electron gyro frequency is $f_{ce} \approx$ 4,200 Hz and the electron plasma frequency $f_{pe} \approx$ 220,000 Hz, such that $f_{pe}/f_{ce} \approx 52$.

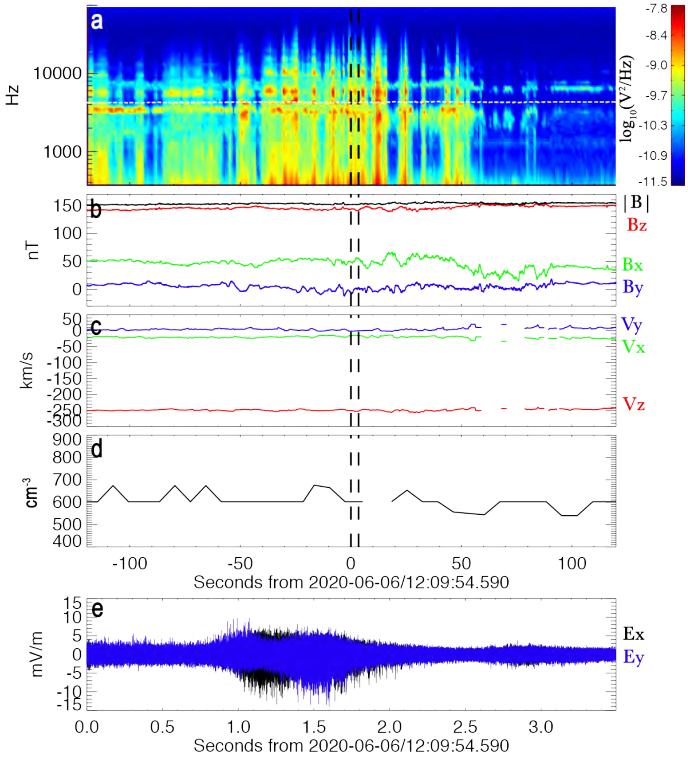

Fig. 1. Context plasma and magnetic field conditions for the studied interval of near-f_{ce} waves. (a) Spectrogram of the differential voltage signals (V_{12} + V_{34}). The dashed white line indicates the local electron cyclotron frequency. The dashed vertical black lines indicate the studied burst interval. (b,c) Ambient magnetic field vector and plasma flow velocity, in the spacecraft frame, in spacecraft coordinates. (d) electron density determined via quasithermal nose measurements. (e) burst capture electric field time series, in spacecraft coordinates.

Figure 2 shows spectrograms (8,192 samples / spectra) of the burst data in Figure 1e. Here, the spectrogram frequencies are normalized to f_{ce}. Figure 2a shows the data between 0 and 10 f_{ce}, while Figure 2b shows the spectral power, summed across the burst, at each frequency in Figure 2a. Figure 2c and Figure 2d show the same data, but only between 0 and 1.5 f_{ce}. The SCM burst data show no signal discernible from noise during this burst capture.

Several wave modes can be identified in these data. In Figure 2a, b, wave power between electron cyclotron harmonics up to at least the 7th harmonic are visible. The strongest wave power for this mode occurs 1 $f_{ce} < f < 2\ f_{ce}$, and successively higher frequencies have lower power. These signals do not appear at integer multiple frequencies of each other. Instead, they appear at variable frequencies between $(N)\ f_{ce} < f < (N+1)\ f_{ce}$. These properties are consistent with electron Bernstein waves (Bernstein 1958). Electron Bernstein waves have been reported in the Earth's magnetopause (Li et al. 2020), near an interplanetary shock (Wilson et al. 2010), at the Earth's bow shock (Breneman et al. 2013) and within the Earth's magnetosphere (e.g. Christiansen et al. (1978)). In the inner terrestrial magnetosphere, these waves are often referred to as electron cyclotron harmonic (ECH) waves (e.g. Zhou et al. (2017) and references therein). Electron Bernstein waves have been observed in the non-shocked solar wind before, but associated with spacecraft charged particle release (Baumgaertel and Sauer 1989). The presence of such waves in the open near-Sun solar wind is a novel observation. Through the rest of this publication, we refer to the electron Bernstein waves as 'Type A' waves. The Type A wave power in the frequency range $f_{ce} < f < 2f_{ce}$ has a center frequency of ~ 5050 Hz, with a bandwidth of ~ 1500 Hz, corresponding to a bandwidth ($\delta f/f$) of ~ 31%.

Two other distinct wave modes are visible in Figures 2c and 2d. The higher frequency wave is designated 'Type B', and the lower frequency wave 'Type C'. Both are narrowband and show time-variable frequencies, leading to summed power spread over a range of frequencies. When wave power is averaged over significant fractions of a second (as in the survey power spectra), these are the waves producing the wave power peaks near ~1.0 f_{ce} (Type B) and ~0.7 f_{ce} (Type C), in the statistical results reported by Malaspina et al. (2020). The significant spread in frequencies reported in Malaspina et al. (2020) is consistent with time-variable frequencies of these waves. Properties of Type B and Type C waves are explored below.

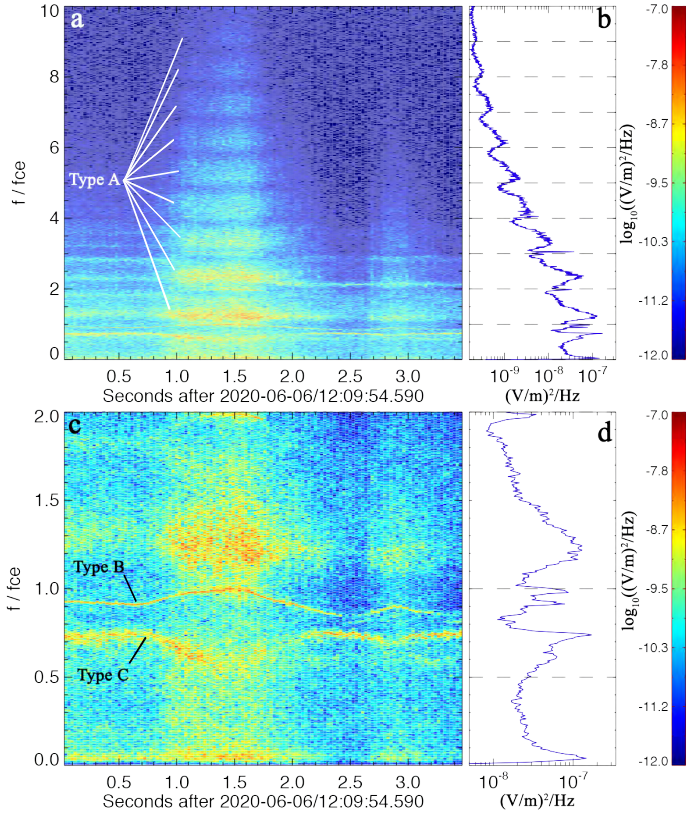

Fig. 2. Spectrograms of the high cadence electric field data from Figure 1e. (a) Fourier spectrogram of electric field data, with frequencies normalized to the local f_{ce}. (b) Sum of power spectral density at each frequency over the ~ 3.5s burst interval. Horizontal dashed lines show integer multiples of f_{ce}. (c,d) Same data as (a,b), but spanning a narrower frequency range.

3.1. Type B: Extremely Narrowband fce Waves

The Type B waves shown in Figure 2c are extremely narrow band, with a bandwidth of $\delta f/f \approx 3\%$. These waves vary in frequency with time across the burst, but do not exceed f_{ce}.

The wave frequency is observed to scale almost linearly with variation in the angle between the background magnetic field and the solar wind velocity ($\theta_{B,Vsw}$). Figure 3a shows $\theta_{B,Vsw}$ across the burst event. Here, the magnetic field data from the FGM is down-sampled to one value per spectra (~0.055 s). Proton velocity moments are determined at a much slower cadence than the fields data are sampled, so the closest (in time) proton velocity moment is used for the solar wind velocity. The proton velocity is steady during this interval (Figure 1). Figure 3b reproduces the burst data electric field power spectra, but with a different color scheme to emphasize the Type B and Type C wave power peaks. The Type B spectral peak for each 8,192-sample spectra is indicated using asterisk symbols, shifted down by ~200 Hz so that both the narrow Type B peak and the symbols can be shown. Gaps indicate times when the signal to noise ratio of the Type B peak fell below 10. The symbols corresponding to different times are colored differently. Figure 3c plots the Type B observed peak frequency (in radians/s, ω_{obs}) as a function of $cos(\theta_{B,Vsw})$. The colors match those in Figure 3b, and at least three intervals with distinctly different slopes are visible.

Given the lack of significant magnetic field structure during this event (Figure 1b, Figure 3a), and the lack of observational evidence for a significant electron flow during the event under study, we conclude that any Doppler shift of wave frequencies must be due to a combination of solar wind flow speed and spacecraft motion. Wave frequency variation due Doppler shift is given by $\omega_{obs} = \omega_{plasma} + |k||V_{sw}|cos(\theta_{k,Vsw})$, where ω_{obs} is the observed wave frequency, $|k|$ is the magnitude of the wave vector, $|V_{sw}|$ is the solar wind speed in the frame of the spacecraft, ω_{plasma} is the proton-frame wave frequency, and $\theta_{k,Vsw}$ is the angle between the wave vector and the plasma flow in the frame of the spacecraft. In the case that ω_{plasma}, $|k|$, and $|V_{sw}|$ are stable over the ~ 3.5s observation time, any change in ω_{obs} should be due to variation in $cos(\theta_{k,Vsw})$. Further, if $\mathbf{k}$ is approximately fixed with respect to $\mathbf{B}$ over this burst interval, then ω_{plasma} should vary linearly with $\theta_{B,Vsw}$. That is, as the ambient magnetic field direction fluctuates, the wave frequency should also fluctuate. Further, if the stated assumptions hold, then a linear fit to ω_{obs} vs. $cos(\theta_{k,Vsw})$ yields an offset corresponding to the plasma frame frequency (ω_{plasma}) and a slope corresponding to $|k||V_{sw}|$. If the angle between $\mathbf{k}$ and $\mathbf{B}$ were known, one could determine this linear fit.

While the burst examined so far is consistent with Doppler shift as the origin of the frequency variation, a second example shown in Figure 4 demonstrates the effect more clearly. Figure 4 has a nearly identical format to Figure 3, for an event recorded near January 29, 2020, 17:15:47 UTC. In Figure 4b, the symbols indicating the identified spectral peaks are shifted upward by 600 Hz so that the Type B spectral line is visible. Type B spectral peaks cannot be clearly separated from other wave power near f_{ce} after ~1.7 seconds into the event. At this time, a coherent low-frequency ion scale wave was present, causing perturbations in $\theta_{B,Vsw}$. The corresponding frequency variation of ω_{obs} is striking, and the fit to the data in ω_{obs}- $cos(\theta_{B,Vsw})$ space is linear.

3.1.1. Type B Doppler Shift Fitting

Returning to the data shown in Figure 3, estimates of $|k|$ and ω_{plasma} can be made, using the frequencies indicated in Figure 3a

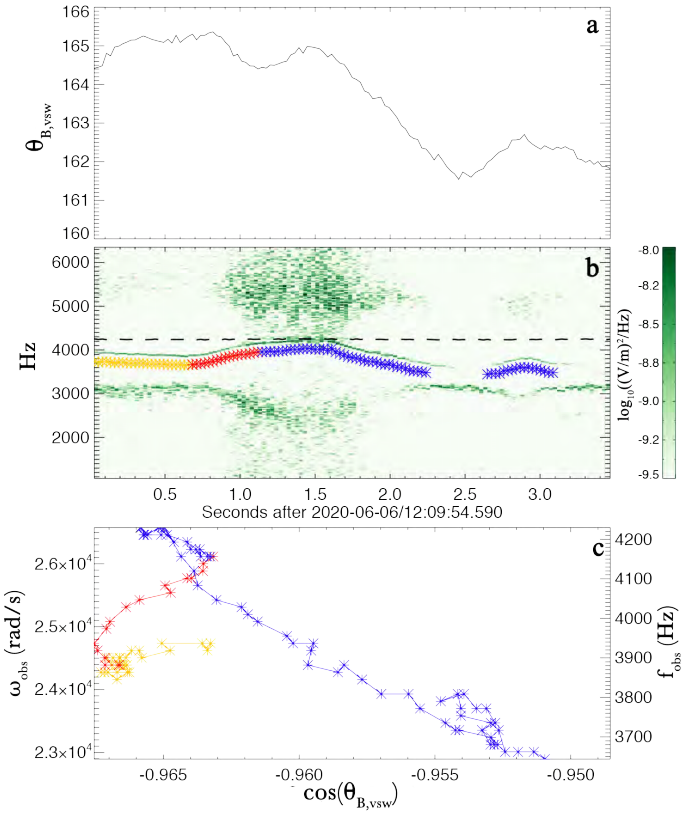

Fig. 3. Initial Doppler analysis for burst data recorded near 2020-06-06/12:09:54 UTC. (a) Angle between the ambient magnetic field vector ($\mathbf{B}$) and the proton flow vector ($\mathbf{V}_{sw}$). (b) Electric field spectrogram, with color scale selected to highlight the Type B wave power. Colored symbols indicate peak Type B frequency for each spectra, plotted with an offset from the Type B spectral line so that both are visible. Orange, red, and blue symbols correspond to three distinct slopes observed in (c). The black dashed line indicates the local electron cyclotron frequency. (c) Observed Type B wave frequency (radians/s) as a function of the cosine of the angle shown in (a).

and the following procedure: $\mathbf{B}$ and $\mathbf{V}_{sw}$ vectors are used to construct an orthonormal coordinate basis defined by $(\mathbf{B}\times\mathbf{V}_{sw})\times\mathbf{B}$, $\mathbf{B}\times\mathbf{V}_{sw}$, and $\mathbf{B}$. In this coordinate basis, the magnetic field vector is $\mathbf{B} = [0, 0, 1]$, and the solar wind velocity vector is $\mathbf{v}_{sw} = [0.31, 0, -0.95]$. A range of possible unit vectors $\hat{k}$ are defined using the polar angle θ and azimuthal angle ϕ. Each angle pair (θ, ϕ) defines a direction of $\hat{k}$ with respect to $\mathbf{B}$ in each spectral window, such that $k_{(BxVsw)xB} = sin(\theta)cos(\phi)$, $k_{(BxVsw)} = sin(\theta)sin(\phi)$, and $k_{(B)} = cos(\theta)$. With these angle definitions, the solar wind vector corresponds to $[\theta, \phi] = [161.8^o, 0^o]$. These angles are defined such that $\theta = 0$ ($\theta = 180$) points parallel (anti-parallel) to $\mathbf{B}$, and $\phi = +90$ points along $+\mathbf{B}\times\mathbf{V}_{sw}$.

Given a $\hat{k}(\theta, \phi)$ and the measured V_{sw}, the quantity $cos(\theta_{k,Vsw})$ can then be determined. The Doppler shift equation ($\omega_{obs} = \omega_{plasma} + |k||V_{sw}|cos(\theta_{k,Vsw})$) can be written as a simple linear equation $y = b + mx$. Here, y is the Type B ω_{obs} in each spectral window. A least absolute deviation linear fit to the plot of y vs. x yields a slope ($m = |k||V_{sw}|$) and an intercept ($b = \omega_{plasma}$). By sweeping through all possible directions of $\hat{k}$, performing such a linear fit for each one, values of ω_{plasma} and $|k|$ can be determined across (θ, ϕ) space.

Figure 5 shows the ranges of ω_{plasma} and $|k|$ that result from applying this procedure to the later part of the wave in Figure 3a (indicated by blue symbols). In Figure 5, regions of (θ, ϕ) space

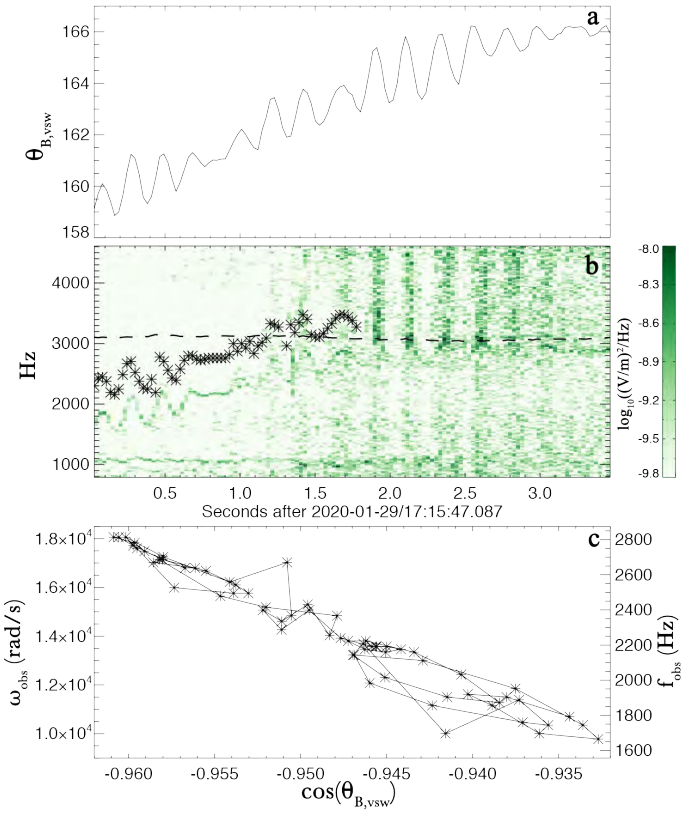

Fig. 4. Same format as Figure 3, but for a burst event recorded near 2020-01-29/17:15:47 UTC. For this event, the frequency peak symbols are not color coded, and they are offset upward in frequency for plotting.

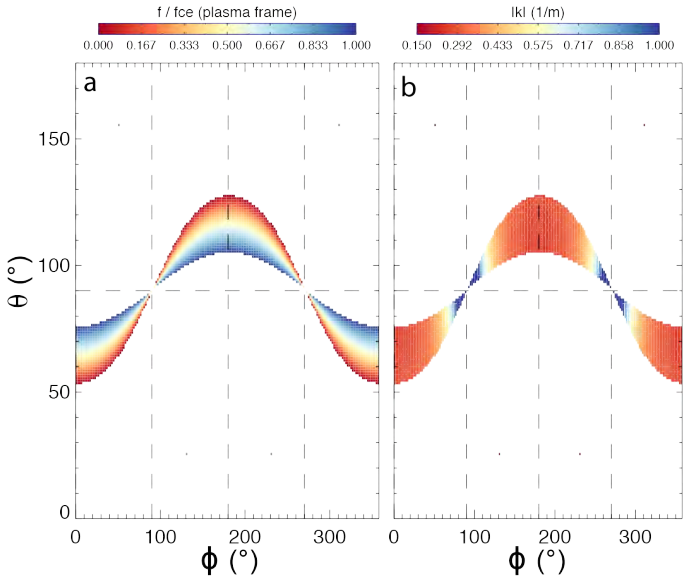

Fig. 5. Doppler analysis output for the data points colored blue in Figure 3. (a) Wave frequency, normalized to f_{ce}, and (b) wave number, in 1/m, both as a function of the angles θ and ϕ as defined in the text. Solutions with $|f| > f_{ce}$ are not plotted.

that yield $\omega_{plasma} > \omega_{ce}$ were removed from consideration. The fit output for f_{plasma}/f_{ce} is shown in Figure 5a and fit output for $|k|$ is shown in Figure 5b.

Type B wave frequencies, in the spacecraft frame, are not observed to exceed the local f_{ce} in this wave event or any of the others examined thus far. If the plasma frame frequency is near f_{ce}, then such asymptotic behavior can be understood as indicating times when the Doppler shift becomes small. If the plasma frame frequency is much greater than f_{ce}, then the observed asymptotic behavior would require a Doppler shift sign and magnitude that always produces $f \leq f_{ce}$ in the spacecraft frame. Given the natural variation of $\mathbf{v}_{sw}$ and $\mathbf{k}$ between wave event observations, this is unlikely. Therefore we exclude solutions with $f > f_{ce}$.

Negative frequency solutions are also excluded. A negative plasma frame frequency corresponds to a polarization change between the spacecraft frame (positive frequency) and the plasma frame. However, the observed Doppler shifts are small relative to a wave with a plasma frame frequency near fce (considering again that the observed Type B frequencies asymptote to $f = f_{ce}$). Such small Doppler shifts are inconsistent with reversal in polarization between the plasma frame and the spacecraft frame.

For the range of f_{plasma} considered, the wave vector $\mathbf{k}$ is oblique, with $50^o < \theta < 130^o$. Given the Debye length ($\sim$ 1.9m) and electron gyro radius (~97 m), smaller values of $|k|$ are more physically reasonable: $|k| = 0.15$ (1/m) corresponds to a wavelength of $\lambda \approx 42$m. Requiring smaller values of $|k|$ place $\mathbf{k}$ within $\sim 30^o$ of perpendicular to the plane defined by $\mathbf{B}$ and $\mathbf{V}_{sw}$. If f_{plasma} remains close to f_{ce} (small Doppler shift), then the wave is even more oblique (θ closer to 90^o).

Figure 6 shows similar fit output to Figure 5, but for the earlier part of the wave in Figure 3a (indicated by red symbols). For these data, the wave vector $\mathbf{k}$ is most oblique for f_{plasma} far from f_{ce}, and slightly less oblique for f_{plasma} near f_{ce}. The fit output values of $|k|$ are similar to those determined in Figure 5, but slightly larger. The fit outputs from Figure 5 and Figure 6 overlap along the region of (θ, ϕ) space where $f_{plasma} \approx f_{ce}$.

One can now make another assumption: that the waves from the earlier and later parts of the burst have similar plasma-frame frequency (f_{plasma}). If this is true, then the true $\hat{k}$ is localized to the (θ, ϕ) region where Figure 5 and Figure 6 overlap, that is, along the dark blue region of Figure 5a and Figure 6a. Combined with the estimate that smaller values of $|k|$ are more physically reasonable, the following properties are now determined for the Type B wave: (i) the wavelength is $21 < \lambda < 42$ m, given $0.15 < |k| < 0.3$ 1/m, (ii) the wave vector is oblique, such that $\hat{k}$ is $\sim 70^o$ from $\mathbf{B}$, (iii) $\hat{k}$ is $\sim 60^o$ from the plane defined by $\mathbf{B}$ and $\mathbf{V}_{sw}$, (iv) the plasma frame frequency (f_{plasma}) is within $\sim$ 20% of the local f_{ce}. These are specific wave properties that can be useful to identify the wave mode.

3.1.2. Type B Resonant Velocities

The wave properties estimated above can be used to estimate the portion of the electron distribution function with which the Type B waves resonate. In the case of Landau resonance, the resonant portion of the distribution can be determined using $\omega_{plasma} = \mathbf{v} \cdot \mathbf{k}$. The component of the Landau resonance parallel to $\mathbf{B}$ satisfies $v_{\|} = \omega_{plasma}/(\,|k|\ cos(\theta_{k,B})\,)$. The analysis in the prior section concluded that $\omega_{plasma} \approx \omega_{ce}$ and $\hat{k} \approx 20^o$ from perpendicular to $\mathbf{B}$, therefore $cos(\theta_{k,B}) \approx cos(70^o) \approx 0.17$. Using these values and $0.15 < |k| < 0.3$ (1/m) results in resonant velocities that correspond to electron energies ($\mathcal{E}$) of $0.19eV < \mathcal{E}_{\|} < 0.75\ eV$. The component of the Landau resonance perpendicular to $\mathbf{B}$ satisfies $v_{\perp} = \omega_{plasma}/(\,|k|\ sin(\theta_{k,B})\,)$, and results in resonant energies of $0.025eV < \mathcal{E}_{\perp} < 0.10eV$. In either case, these

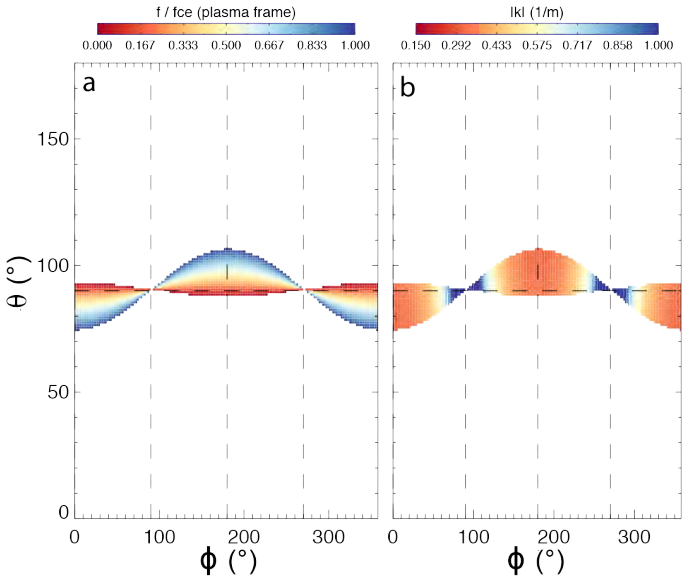

Fig. 6. Doppler analysis output for the data points colored red in Figure 3. Same format as Figure 5. Solutions with $|f| > f_{ce}$ are not plotted.

resonant energies are low, near the center of the core electron velocity distribution function.

In the case of cyclotron resonance, the resonant portion of the distribution can be determined using $\omega_{plasma} = \mathbf{v}\cdot\mathbf{k} + N\omega_{ce}$, where N is a positive or negative integer and $\omega_{ce} = 2\pi f_{ce}$. Cyclotron resonant velocities satisfy $\mathbf{v}_{\|} = (\omega_{plasma} - N\omega_{ce})/(\,|k|\,cos(\theta_{k,B})\,)$. Because $\omega_{plasma} \approx \omega_{ce}$, and the goal is to obtain approximate resonant energies, the assumption $\omega_{plasma} = 0.98\ \omega_{ce}$ is used here, but is only important for the $N = \pm 1$ cyclotron resonances. Using all other assumptions from the Landau case, the $N = 1$ cyclotron resonance produces $0.00007eV < \mathcal{E}_{\|} < 0.0003eV$, and $N = -1$ produces $0.74eV < \mathcal{E}_{\|} < 3.0eV$. Extending to $N = \pm 2$ results in $0.2eV < \mathcal{E}_{\|} < 0.8eV$ and $1.7eV < \mathcal{E}_{\|} < 6.7eV$, for positive and negative cases respectively. All resonant energies discussed are in the plasma frame.

The $-N$ resonances correspond to electron energies further from the center of the electron core distribution, which may be more realistic for these waves given the ~ 38eV electron core temperature. In this formulation, negative values of N correspond to the anomalous cyclotron resonance. With anomalous cyclotron resonance, the resonant electrons' guiding center velocities are parallel to a component of the wave vector. For this case specifically, **B** points within $\sim 20^o$ of sunward, and the Doppler shift is such that Type B wave frequencies drop, so the Type B wave vector points generally along **B** (sunward, against the solar wind flow). Therefore, the resonant electrons guiding center velocities are likely sunward, implying that Type B waves are resonant with a portion of the sunward core electron distribution.

3.2. Type C: Moderately Narrowband f_{ce} / 2 Waves

The Type C waves shown in Figure 2c are moderately narrow band, with a bandwidth of $\delta f/f \approx 12\%$. These waves vary in frequency with time across the burst, but do not fall below $f_{ce}/2$. Similar to the Type B waves, the Type C frequency variation scales approximately linearly with variation in $\theta_{B,Vsw}$. Strikingly, the frequency variation of Type C waves mirrors that of Type B waves (Figure 2). Where Type B waves decrease in frequency, Type C increase, and vice versa. When Type B waves asymptote to f_{ce}, Type C waves simultaneously asymptote to $f_{ce}/2$. The mirrored Doppler shift suggests that the component of the wave vector along the solar wind direction for these two wave types is oppositely directed. The Type B wave vector appears to have a component toward the Sun (Doppler frequency decrease), while the Type C wave vector has a component away from the Sun (Doppler frequency increase). This mirrored Doppler shift behavior is consistently observed in all of the half dozen burst data events examined in detail where both Type B and Type C waves are distinct (other events not shown here). A statistical study is required to explore this behavior more generally, but is beyond the scope of the present work.

The same Doppler shift fitting analysis that was applied to the Type B waves can be applied to the Type C waves, but with additional uncertainty in the results because the spectral peak frequency of the Type C waves is not sufficiently distinct near the central region of this event, where the strongest variation in frequency occurs. Also, Type C waves are not as narrow band as Type B waves, producing additional frequency scatter that makes fits to the ω_{obs} vs. $cos(\theta_{k,Vsw})$ data more uncertain.

Figure 7 has the same format as Figure 6, but shows results for Type C frequency peaks from the second part of the burst event (after the most intense cyclotron power). Following similar reasoning to the Type B analysis, the following properties are determined for the Type C wave: (i) $0.08 < |k| < 0.15$ 1/m, (ii) a wave vector with $\hat{k} \approx 5^o$ from perpendicular to **B**, (iii) $\hat{k}$ less than $\sim 30^o$ from perpendicular to the plane defined by **B** and $\mathbf{V}_{sw}$, (iv) a plasma frame frequency (f_{plasma}) within ~ 20% of $f_{ce}/2$.

Considering Landau resonance for Type C waves, using $cos(\theta_{k,B}) \approx cos(85^o)$ and $0.08 < |k| < 0.15$ (1/m), one finds that $3eV < \mathcal{E}_{\|} < 10eV$ and $0.02eV < \mathcal{E}_{\perp} < 0.08eV$. With cyclotron resonance, these values produce $0.80eV < \mathcal{E}_{\|} < 2.9eV$ for $N = 1$, and $6.5eV < \mathcal{E}_{\|} < 23.0eV$ for $N = -1$. For Type C waves, as was determined for Type B waves, all estimated resonant energies are low, near the center of the electron core distribution. Again, all resonant energies discussed are in the plasma frame.

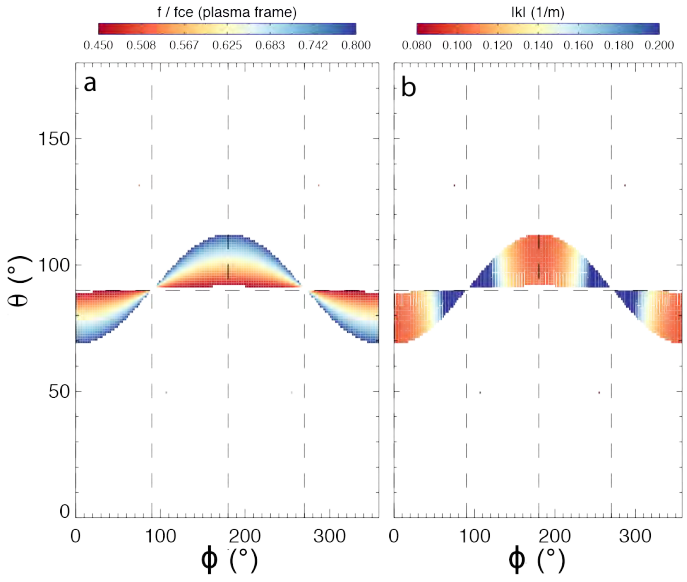

Fig. 7. Doppler analysis output for the Type C frequency peaks after the most intense cyclotron power. Same format as Figure 5. Solutions outside the range $0.45f_{ce} < |f| < 0.8f_{ce}$ are not plotted.

3.3. Type B and Type C Polarization

Polarization is another useful piece of information to help identify wave modes. Polarization determination in this case is somewhat hampered by having only two reliable electric field measurement directions (in plane of the heat shield), but much can still be determined.

Figure 8a shows the wave power spectrogram of the burst under study. Horizontal dashed lines indicate f_{ce} and $f_{ce}/2$. The vertical solid lines indicate the central region, where Type A wave power maximizes. Figure 8b and Figure 8c show the results of a cross-spectral analysis conducted on the two electric field signals shown in Figure 1e. These signals are orthogonal, since they are rotated into spacecraft coordinates. A filter has been applied such that any cross-spectral result spectral bin with wave power below 2×10^{-10} $(V/m)^2/Hz$ is not plotted. This is done to isolate the Type A, Type B, and Type C waves. The cross-spectral analysis was conducted in the plane of the heat shield, since only those two signals are well-calibrated for this event.

Figure 8b shows a spectrogram of degree of polarization. All three wave types show a high degree of polarization, indicating strong coherence between the two input signals. Figure 8c shows a spectrogram of wave ellipticity, defined as the ratio of the minor axis to the major axis for the ellipse transcribed in the plane of the heat shield by the signal in each spectral bin. Red colors correspond to right handed polarization, blue colors to left-handed polarization. The maximum magnitude of calculated polarization is $\sim$ 0.7, indicating elliptical polarization in the plane of the heat shield.

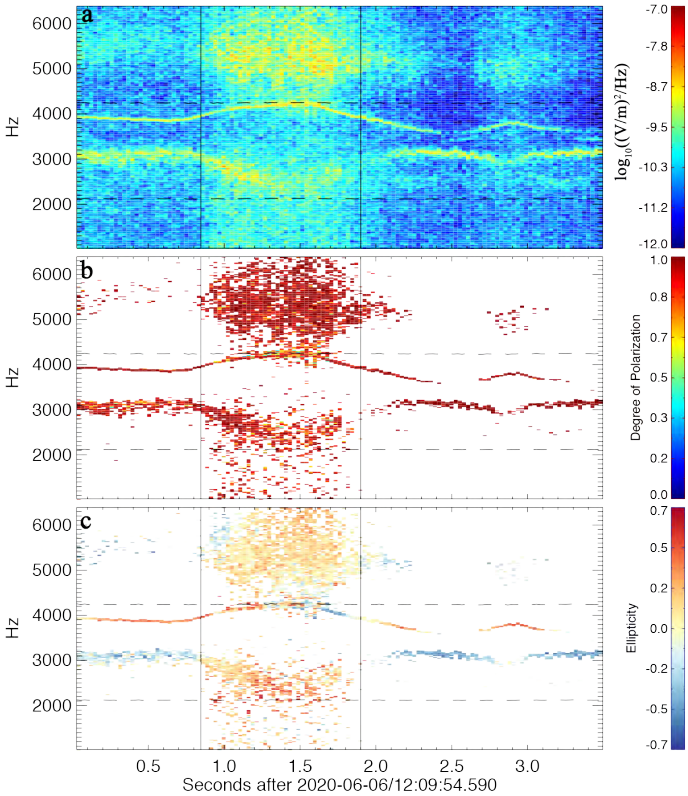

Fig. 8. Type B and Type C cross-spectral analysis. (a) Electric field spectrogram near f_{ce}. Dashed horizontal lines indicate f_{ce} and $f_{ce}/2$. (b) Degree of polarization spectrum from cross-spectral analysis. (c) Wave ellipticity spectrum from cross-spectral analysis. Vertical lines indicate the region of strongest Type A wave power.

From Figure 8c, it can be seen that Type A waves are right-hand polarized, consistent with the interpretation that these are electron Bernstein waves. Outside the central region, the Type A polarization is mixed and difficult to determine given the relatively low wave power in these signals. Type B waves are right-hand polarized outside the central region, and Type C waves are left-hand polarized outside of the central region. Within the central region, Type B and Type C signals become more ambiguous. Type B and Type C wave frequencies go to f_{ce} and $f_{ce}/2$, respectively, in the central region. The degree of polarization falls for Type B waves, and the ellipticity becomes scattered, at times appearing left hand polarized. This is difficult to interpret physically, as the Type A and Type B signals become mixed during this interval. The Type C polarization changes to right-handed within the central region, as the wave power becomes much more diffuse in frequency, and a distinct spectral peak is not observed. This too is difficult to interpret physically, as the Type C signals become mixed with other wave power present during this interval near $f_{ce}/2$.

4. Discussion

From the above analysis, Type B waves have the following properties: (i) a plasma-frame frequency near f_{ce}, (ii) right-hand elliptical polarization, (iii) wave vector magnitude of $0.15 < |k| < 0.3$ 1/m, (iv) wave vector direction $\sim 20^o$ from perpendicular to **B** with a sunward component on either side of the central region, (v) resonance with low energy electrons, close to the center of the electron core distribution, possibly anomalous cyclotron resonance, and (vi) frequency variation (presumed due to Doppler shift) which mirrors that of the Type C waves.

Type C waves have the following properties: (i) a plasma-frame frequency near $f_{ce}/2$, (ii) left-hand elliptical polarization, (iii) wave vector magnitude of $0.08 < |k| < 0.15$ 1/m, (iv) wave vector direction $\sim 5^o$ from perpendicular to **B** with an anti-sunward component on either side of the central region, (v) resonance with low energy electrons, close to the center of the electron core distribution, possibly anomalous cyclotron resonance, and (vi) frequency variation (presumed due to Doppler shift) which mirrors that of the Type B waves.

Given these properties, as well as the amplitude variation of Type A (electron Bernstein) waves across the burst event, we conclude that the central region is likely a source region for all three types of wave. This conclusion is based on the observation that Type A (electron Bernstein) wave power maximizes in this region, and the observation that Type B and Type C wave frequencies asymptote to $\sim$ f_{ce} and $\sim$ $f_{ce}/2$ in this region. If this is a source region, then waves will generally radiate away from it. But one needs to reconcile this concept with the observation that the Doppler shift for both Type B and Type C waves has the same sense (down for Type B, up for Type C) on either side of the source region. The source region is assumed to be a cylinder. This assumption is based on the gyrotropic nature of electrons in the ambient solar wind, combined with the observed lack of magnetic field structure at the time when the Type A wave power maximizes (less than 1 degree variation of the magnetic field vector, see Figure 3a).

If the source region is cylindrical and elongated along **B**, then the combined solar wind and spacecraft velocity cause the structure to pass over the spacecraft at a small angle relative to the source region long axis. If the Type B wave vectors are tilted everywhere along **B** (in a cone opening generally sunward), then the sign of the $\mathbf{k} \cdot \mathbf{V}_{sw}$ Doppler shift term on either side of the source region would be negative, consistent with Figure 2b. Sim-

ilarly, if the Type C wave vectors are tilted everywhere against **B** (in a cone opening generally anti-sunward), then the sign of the $\mathbf{k} \cdot \mathbf{V}_{sw}$ Doppler shift term on either side of the source region would be positive, also consistent with Figure 2b. Further, if the Type A (electron Bernstein) wave vectors were close to perpendicular with **B**, but radially outward from the cylindrical source region, then the Type A frequency would be slightly higher at the start of the event and slightly lower at the end of the event. There is an indication of this behavior in Figure 2b, comparing the frequencies of Type A wave power near 0.5 s (~1.3 f_{ce}) and near 3 s (~1.15 f_{ce}). The schematic cartoon in Figure 9 summarizes this source region concept. Here, the cones indicate the relative wave vector direction for each type of wave, but all types of wave are meant to originate from points along the full length of the source region cylinder.

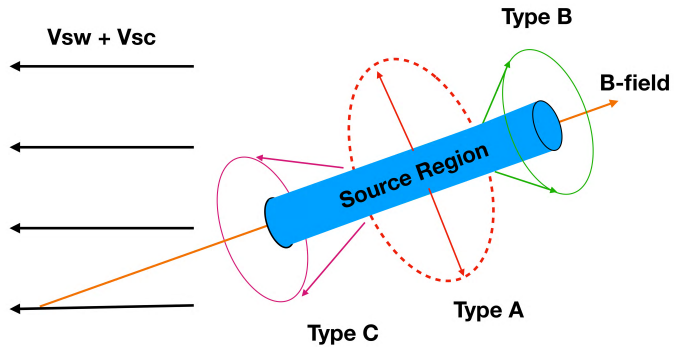

Fig. 9. Cartoon schematic of the observed near-f_{ce} source region.

The estimated wavenumber ranges and orientations for Type B and Type C waves allow estimates of plasma-frame wavelengths. For Type B, $61 < \lambda_{\parallel} < 122$ m, and $22 < \lambda_{\perp} < 45$ m. For Type C, $480 < \lambda_{\parallel} < 901$ m, and $42 < \lambda_{\perp} < 79$ m. All of these estimated wavelengths are one to two orders of magnitude longer than the Debye length ($\lambda_D \sim 1.9m$). The perpendicular wavelengths are similar to fractions of the electron gyro radius ($\rho_e \sim 97$ m) such that for Type B $1/4\rho_e < \lambda_{\perp} < 1/2\rho_e$, and for Type C $1/2\rho_e < \lambda_{\perp} < 1\rho_e$.

Both Type B and Type C parallel wavelengths are significantly smaller than the lower bound source region extent along **B**, a necessary condition for wave growth in this region. The source region is observed for ~ 1s. Assuming that it is embedded in the solar wind flow, it is moving ~ 250 km/s radially away from the Sun in the frame of the spacecraft. Assuming that it extends along **B**, and accounting for the 163^o angle between **B** and $\mathbf{V}_{sw}$, the lower bound source region extent along **B** is ~ 260 km, much larger than the estimated parallel wavelengths.

A comparison of the observations and the source region picture presented above shows at least one unresolved discrepancy. If Type B waves have a plasma frame frequency close to f_{ce}, and they are resonant with electrons, then they should be right-hand polarized in the plasma frame. If Type B waves have a sunward wave vector (consistent with anomalous cyclotron resonance, discussed in section 3.1.2), then Doppler shift will reduce their observed frequency by a small amount relative to their plasma frame frequency. With these properties ($\omega_{plasma} \approx \omega_{fce}$, sunward $\hat{k}$, small Doppler shift), Type B waves should be right-hand polarized in the spacecraft frame. This is consistent with the observed polarization in Figure 8.

However, if Type C waves have a plasma frame frequency close to $f_{ce}/2$, and they too are resonant with electrons, then they should also be right-hand polarized in the plasma frame. If Type C waves have an anti-sunward wave vector, consistent with a Doppler shift up in frequency, by an amount small compared to their plasma frame frequency, then one expects that Type C waves will also be right hand polarized in the spacecraft frame. Yet the observed polarization in Figure 8 indicates left-hand. This discrepancy remains unresolved, and likely requires a study that treats more than one burst event.

For both events presented here, the Type B wave frequency in the spacecraft frame approaches the electron cyclotron frequency in the source region, where the wave emission is strongest. If our Doppler shift interpretation of the wave frequency variation in time is correct, then why should the Doppler shift consistently minimize in the source region, where presumably the **k** and $\mathbf{v_{sw}}$ vectors have an arbitrary orientation from event to event?

The physical quantities that produce Doppler shift are $|v_{sw}|$, $|k|$, and $cos(\theta_{k,vsw})$. Inside and outside the source region, we know that $|v_{sw}|$ is steady to our ability to measure it, and $cos(\theta_{k,vsw})$ should be somewhat arbitrary from event to event. Although $cos(\theta_{k,vsw})$ is not completely arbitrary, as the waves under study only appear when $\mathbf{v_{sw}}$ is within ~ 20^o of parallel to radially outward from the Sun (Malaspina et al. 2020).

This leaves the possibility that $|k|$ may be smaller inside the source region than outside. This could reduce the Doppler shift in the source region, and bring the wave frequency closer to its plasma frame value. There is some observational support for this. Looking at the blue points in Figure 3c, there is a small cluster of points in the upper left, where the slope of the best-fit line would be shallower than the slope of the best-fit line to the majority of the blue points. This cluster of points corresponds exactly to the points in the center of the source region. A linear fit to these points alone, for any value of θ, ϕ produces a slope, and therefore $|k|$, which is smaller by ~ 40% than the $|k|$ determined using the rest of the blue points. However, only this one event has been examined to this level of detail, and we do not yet know if a smaller $|k|$ in the source region is a consistent property of these waves.

A second change in the wave spectra also occurs in the strong emission (source) regions: the wave bandwidth increases. This behavior can be seen in Figure 2c near 1.3 seconds and is observed for Type A, Type B and Type C waves. The waves created in the a region should produce a distribution of wave vectors within the source region that is more isotropic with respect to the background magnetic field direction compared to the distribution of wave vectors outside of the source region. The more isotropic the distribution of wave vectors is, the broader the wave bandwidth should be, as each wave vector produces a slightly different Doppler shift. This is consistent with the observations.

A broader study is required to determine if these are general behaviors of the wave types studied here.

4.1. Potential Driving Instabilities

The instability or instabilities driving the observed waves are not definitively determined in this analysis, but we discuss some possibilities here. The first is electron cyclotron drift instability (ECDI) (e.g., Forslund et al. 1970, 1971, 1972). The free energy for the ECDI is a cross-field drift between electrons and ions, specifically ions moving across the magnetic field. Waves radiated by this instability are observed as a coupling between electron Bernstein modes and Doppler-shifted ion acoustic waves. The ECDI is highly unlikely to be responsible for the waves studied here as magnetic field field fluctuations are small. Without strong magnetic field gradients, like those at collisionless shocks

for example, it is not clear how to generate a sizeable ion beam moving across the magnetic field relative to the the core ions and electrons moving with the solar wind.

It is also possible to generate cyclotron harmonics with an electron beam drifting across the magnetic field. This instability requires that a fraction of the electrons drift with the $\boldsymbol{E} \times \boldsymbol{B}$- and ∇B-drifts at a magnetic field gradient (e.g., Gary and Sanderson 1970). Again, magnetic field field fluctuations are small during the interval examined here so this instability is not likely to be active.

Another possibility for generating the observed waves is through nonlinear wave-wave interactions. This class of process usually requires a pump wave to amplify or couple to oscillations that mode convert to other daughter modes. Harker and Crawford (1968) showed that a pump wave could generate two daughter waves in a form of traveling wave parametric amplification, one of which would be cyclotron harmonic waves. The daughter waves were expected to have $k\ V_{Te}/\Omega_{ce} \lesssim 3$ but our results suggest values >10. This process requires a very uniform plasma and magnetic field, which is suggestive since the modes investigated here occur during regions of low magnetic turbulence (Malaspina et al. 2020).

A more recent study found that an electromagnetic pump wave can decay into an ion acoustic wave and electrostatic electron Bernstein mode (e.g., Kumar and Tripathi 2006). This study also found that the converse can occur, i.e., an electrostatic electron Bernstein wave in the presence of low frequency, low wavelength ion acoustic wave can generate electromagnetic electron cyclotron harmonics. The expected wave number for the electron Bernstein waves is $k\,\rho_{ce} \sim 2$ while our observations suggest $k\,\rho_{ce}$ > 10 for the Type B waves and >7 for Type C waves.

Another possible candidate is a loss-cone instability (e.g., Ashour-Abdalla and Kennel 1978; Ashour-Abdalla et al. 1979). This instability is expected to grow for $3 \lesssim k\,\rho_{ce,h} \lesssim 15$, where $\rho_{ce,h}$ is the thermal gyroradius of the hot electrons (sunward hot electrons in our work) and higher harmonics are expected at larger values of $k\,\rho_{ce,h}$. The suprathermal electron temperature is typically ~2.5–5.0 times that of the core and total at both 1 AU and as close as 0.17 AU (e.g., Halekas et al. 2020a; Wilson III et al. 2019). Using this range we find $\rho_{ce,h} \sim$ 146–208 m, which gives us $k\,\rho_{ce,h} \sim$ 22–62 for Type B and ~11–31 for Type C, values beyond the range of $k\,\rho_{ce,h}$ where growth is expected. Finally, variations on the loss-cone instability have been performed using a stationary (in the plasma frame) perpendicular ring-beam combined with a core (e.g., Maxwellian) velocity distribution but again the expected wave numbers are $k\,\rho_{ce} \lesssim 3$ (e.g., Hadi et al. 2015).

In the case studied here, a loss cone cannot form in the anti-sunward direction, as the hot electrons in that direction form the strahl beam, which adiabatically narrows as these electrons escape the solar corona (e.g. (Berčič et al. 2020) and references therein). However, at the studied radial distances from the sun, the strahl electron population has only just begun to scatter into the isotropic halo (Halekas et al. 2020b). There is a possibility that a loss cone can form in the sense that the sunward portion of the halo may not yet be populated (via strahl scattering) at these radial distances. While the SPANe instrument does have an unobstructed field of view in the anti-sunward direction, the angular resolution in that direction is limited, which would not allow the detection of a loss cone if it was narrower than $\sim 20^o$. Further, the analysis presented earlier indicates that the Type B and Type C waves are resonant with electrons at much lower energies than those active in a loss cone instability as discussed here.

Only some of the above possibilities can explain one of the more difficult issues pertaining these observations, the polarizations. There are no known instabilities that would generate electron-scale fluctuations in this frequency range with a left-hand polarization. That is, none of the above instabilities could generate an intrinsically left-hand polarized oscillation with wavelengths at or below the electron gyroscale. The only potential mode is the ion acoustic wave in its electromagnetic form, but whether it can persist in this frequency range at these wavelengths while still being electromagnetic is not known. A possible source of ion acoustic modes is a nonlinear wave-wave interaction, as discussed above, but these specific processes should generate the electrostatic version of the wave. The expected wavelength of the ion acoustic mode is consistent with the estimates for the Type C waves, however. When the wave normal angle of an ion acoustic wave is large, as estimated here for the Type C waves, then the wave should be electromagnetic not purely electrostatic.

Another complication is that of Doppler-shifting. The left-hand polarization of the Type C mode in the spacecraft frame is clear. The problem is that with our estimates for $k \sim 0.08$–0.15 m^{-1} and the measurement of Vsw ~ 250 km/s, the maximum Doppler-shift possible for the Type C mode is only ~3–6 kHz (i.e., assuming $\theta_{kV} \sim 0°$). However, our estimates of k were derived under constraints that suggested θ_{kV} could be as small as ~50°. Then the Doppler-shift range for Type C waves drops to ~2.0–3.8 kHz. The Type C waves are seen at ~2.5–3.1 kHz in the spacecraft frame, so their rest frame frequencies, were the polarization to be reversed, would need to be <1 kHz. If the Type C waves are intrinsically left-hand polarized, then they must be Doppler-shifted to higher frequencies in the spacecraft frame. However, this poses a problem as we are not aware of a left-hand polarized mode with $k\,\rho_{ce} > 7$, i.e., wavelength well below the thermal electron gyroradius.

5. Conclusions

This study examined high-cadence burst data captures of electric and magnetic fields of near-f_{ce} waves in the near-Sun solar wind. It was determined that these waves correspond to at least three separate, simultaneously occurring, wave modes, referred to as Type A, Type B, and Type C. Type A waves are identified as electron Bernstein waves given the frequency distribution of their prominent harmonics. The modes of the Type B and Type C waves were not conclusively identified, but many of their properties were estimated, including their wave numbers (Type B ~ 0.23 m^{-1}, Type C ~ 0.12 1/m), wave vector direction (Type B ~ 70^o, Type C ~ 85^o, from the ambient B-field direction), polarization (Type B right-hand elliptically polarized, Type C left-hand elliptically polarized, in the frame of the spacecraft), and frequency variation. The two wave types appear to be intimately connected, with opposing frequency variation in time, though with different magnitudes (df / f varies by ~ 10% for Type B waves and ~ 30% for Type C waves across the studied event).. Resonant electron energies were estimated based on observed wave properties, indicating that these waves grow from an instability active near the center of the electron core population. By comparing the frequency and wave vector characteristics of all three waves, a source region geometry was suggested.

While only a single wave burst was examined in detail here, the prior statistical study (Malaspina et al. 2020) demonstrated that these near-f_{ce} waves can persist for minutes to hours, occurring on magnetic field lines close to the theoretical Parker spiral geometry with low fluctuation amplitudes. These near-f_{ce}

waves are only observed in the near-Sun environment, and become stronger and more frequently observed close to the Sun, preferentially occurring when the electron core shows strong Sunward drift.

These properties indicate that these waves grow along field lines most directly connected to the solar corona, which therefore contain electrons that have undergone the least evolution since escaping the corona. Therefore, the waves studied here likely play an important role in the near-Sun evolution of the solar wind electron distribution function, particularly concerning the evolution of the cold core population as it interacts with the escaping strahl electrons.

Acknowledgements. The authors acknowledge helpful conversations with Rudolf Treumann concerning wave growth possibilities and helpful comments from Thierry Dudok de Wit. The authors thank the Parker Solar Probe, FIELDS and SWEAP teams. The FIELDS experiment on Parker Solar Probe was designed and developed under NASA contract NNN06AA01C. All data used here are publicly available on the FIELDS and SWEAP data archives: http://fields.ssl.berkeley.edu/data/,
http://sweap.cfa.harvard.edu/pub/data/sci/sweap/

References

O. V. Agapitov, T. Dudok de Wit, F. S. Mozer, J. W. Bonnell, J. F. Drake, D. Malaspina, V. Krasnoselskikh, S. Bale, P. L. Whittlesey, A. W. Case, C. Chaston, C. Froment, K. Goetz, K. A. Goodrich, P. R. Harvey, J. C. Kasper, K. E. Korreck, D. E. Larson, R. Livi, R. J. MacDowall, M. Pulupa, C. Revillet, M. Stevens, and J. R. Wygant. Sunward-propagating Whistler Waves Collocated with Localized Magnetic Field Holes in the Solar Wind: Parker Solar Probe Observations at 35.7 R$_?$ Radii. *The Astrophysical Journal, Letters*, 891 (1):L20, March 2020. .

M. Ashour-Abdalla and C. F. Kennel. Nonconvective and convective electron cyclotron harmonic instabilities. *J. Geophys. Res.*, 83:1531–1543, April 1978. .

M. Ashour-Abdalla, C. F. Kennel, and W. Livesey. A parametric study of electron multiharmonic instabilities in the magnetosphere. *J. Geophys. Res.*, 84: 6540–6546, November 1979. .

S. D. Bale, K. Goetz, P. R. Harvey, P. Turin, J. W. Bonnell, T. Dudok de Wit, R. E. Ergun, R. J. MacDowall, M. Pulupa, M. Andre, M. Bolton, J. L. Bougeret, T. A. Bowen, D. Burgess, C. A. Cattell, B. D. G. Chandran, C. C. Chaston, C. H. K. Chen, M. K. Choi, J. E. Connerney, S. Cranmer, M. Diaz-Aguado, W. Donakowski, J. F. Drake, W. M. Farrell, P. Fergeau, J. Fermin, J. Fischer, N. Fox, D. Glaser, M. Goldstein, D. Gordon, E. Hanson, S. E. Harris, L. M. Hayes, J. J. Hinze, J. V. Hollweg, T. S. Horbury, R. A. Howard, V. Hoxie, G. Jannet, M. Karlsson, J. C. Kasper, P. J. Kellogg, M. Kien, J. A. Klimchuk, V. V. Krasnoselskikh, S. Krucker, J. J. Lynch, M. Maksimovic, D. M. Malaspina, S. Marker, P. Martin, J. Martinez-Oliveros, J. McCauley, D. J. McComas, T. McDonald, N. Meyer-Vernet, M. Moncuquet, S. J. Monson, F. S. Mozer, S. D. Murphy, J. Odom, R. Oliverson, J. Olson, E. N. Parker, D. Pankow, T. Phan, E. Quataert, T. Quinn, S. W. Ruplin, C. Salem, D. Seitz, D. A. Sheppard, A. Siy, K. Stevens, D. Summers, A. Szabo, M. Timofeeva, A. Vaivads, M. Velli, A. Yehle, D. Werthimer, and J. R. Wygant. The FIELDS Instrument Suite for Solar Probe Plus. Measuring the Coronal Plasma and Magnetic Field, Plasma Waves and Turbulence, and Radio Signatures of Solar Transients. *Space Science Reviews*, 204(1-4):49–82, December 2016. .

S. D. Bale, S. T. Badman, J. W. Bonnell, T. A. Bowen, D. Burgess, A. W. Case, C. A. Cattell, B. D. G. Chandran, C. C. Chaston, C. H. K. Chen, J. F. Drake, T. Dudok de Wit, J. P. Eastwood, R. E. Ergun, W. M. Farrell, C. Fong, K. Goetz, M. Goldstein, K. A. Goodrich, P. R. Harvey, T. S. Horbury, G. G. Howes, J. C. Kasper, P. J. Kellogg, J. A. Klimchuk, K. E. Korreck, V. V. Krasnoselskikh, S. Krucker, R. Laker, D. E. Larson, R. J. MacDowall, M. Maksimovic, D. M. Malaspina, J. Martinez-Oliveros, D. J. McComas, N. Meyer-Vernet, M. Moncuquet, F. S. Mozer, T. D. Phan, M. Pulupa, N. E. Raouafi, C. Salem, D. Stansby, M. Stevens, A. Szabo, M. Velli, T. Woolley, and J. R. Wygant. Highly structured slow solar wind emerging from an equatorial coronal hole. *Nature*, 576(7786):237–242, December 2019. .

K. Baumgaertel and K. Sauer. Interpretation of electron cyclotron harmonic waves observed at an ampte lithium release in the solar wind. *Journal of Geophysical Research*, 94(A9):11983–11988, September 1989. .

Ira B. Bernstein. Waves in a Plasma in a Magnetic Field. *Physical Review*, 109 (1):10–21, January 1958. .

Laura Berčič, Davin Larson, Phyllis Whittlesey, Milan Maksimović, Samuel T. Badman, Simone Landi, Lorenzo Matteini, Stuart. D. Bale, John W. Bonnell, Anthony W. Case, Thierry Dudok de Wit, Keith Goetz, Peter R. Harvey, Justin C. Kasper, Kelly E. Korreck, Roberto Livi, Robert J. MacDowall, David M. Malaspina, Marc Pulupa, and Michael L. Stevens. Coronal Electron Temperature Inferred from the Strahl Electrons in the Inner Heliosphere: Parker Solar Probe and Helios Observations. *The Astrophysical Journal*, 892 (2):88, April 2020. .

Trevor A. Bowen, Alfred Mallet, Jia Huang, Kristopher G. Klein, David M. Malaspina, Michael Stevens, Stuart D. Bale, J. W. Bonnell, Anthony W. Case, Benjamin D. G. Chandran, C. C. Chaston, Christopher H. K. Chen, Thierry Dudok de Wit, Keith Goetz, Peter R. Harvey, Gregory G. Howes, J. C. Kasper, Kelly E. Korreck, Davin Larson, Roberto Livi, Robert J. MacDowall, Michael D. McManus, Marc Pulupa, J. L. Verniero, and Phyllis Whittlesey. Ion-scale Electromagnetic Waves in the Inner Heliosphere. *The Astrophysical Journal Supplement Series*, 246(2):66, February 2020. .

A. W. Breneman, C. A. Cattell, K. Kersten, A. Paradise, S. Schreiner, P. J. Kellogg, K. Goetz, and L. B. Wilson. STEREO and Wind observations of intense cyclotron harmonic waves at the Earth's bow shock and inside the magnetosheath. *Journal of Geophysical Research (Space Physics)*, 118(12):7654–7664, December 2013. .

A. W. Case, Justin C. Kasper, Michael L. Stevens, Kelly E. Korreck, Kristoff Paulson, Peter Daigneau, Dave Caldwell, Mark Freeman, Thayne Henry, Brianna Klingensmith, J. A. Bookbinder, Miles Robinson, Peter Berg, Chris Tiu, Jr. Wright, K. H., Matthew J. Reinhart, David Curtis, Michael Ludlam, Davin Larson, Phyllis Whittlesey, Roberto Livi, Kristopher G. Klein, and Mihailo M. Martinović. The Solar Probe Cup on the Parker Solar Probe. *The Astrophysical Journal Supplement*, 246(2):43, February 2020. .

Cynthia Cattell, Benjamin Short, Aaron Breneman, Jasper Halekas, Phyllis Whittesley, Justin Kasper, Mike Stevens, Tony , Case, Michel Moncuquet, Stuart Bale, John Bonnell, Thierry Dudok de Wit, Keith Goetz, Peter Harvey, Robert MacDowall, David Malaspina, Marc Pulupa, and Goodrich Katherine. Narrowband oblique whistler-mode waves: comparing properties observed by Parker Solar Probe at <0.3 AU and STEREO at 1 AU . *Astronomy and Astrophysics*, January 2021. .

C. C. Chaston, J. W. Bonnell, S. D. Bale, J. C. Kasper, M. Pulupa, T. Dudok de Wit, T. A. Bowen, D. E. Larson, P. L. Whittlesey, J. R. Wygant, C. S. Salem, R. J. MacDowall, R. L. Livi, D. Vech, A. W. Case, M. L. Stevens, K. E. Korreck, K. Goetz, P. R. Harvey, and D. M. Malaspina. MHD Mode Composition in the Inner Heliosphere from the Parker Solar Probe's First Perihelion. *The Astrophysical Journal Supplement Series*, 246(2):71, February 2020. .

C. H. K. Chen, S. D. Bale, J. W. Bonnell, D. Borovikov, T. A. Bowen, D. Burgess, A. W. Case, B. D. G. Chandran, T. Dudok de Wit, K. Goetz, P. R. Harvey, J. C. Kasper, K. G. Klein, K. E. Korreck, D. Larson, R. Livi, R. J. MacDowall, D. M. Malaspina, A. Mallet, M. D. McManus, M. Moncuquet, M. Pulupa, M. L. Stevens, and P. Whittlesey. The Evolution and Role of Solar Wind Turbulence in the Inner Heliosphere. *Astrophys. J. Suppl.*, 246(2):53, February 2020. .

P. Christiansen, P. Gough, G. Martelli, J. J. Bloch, N. Cornilleau, J. Etcheto, R. Gendrin, D. Jones, C. Beghin, and P. Decreau. Geos I - Identification of natural magnetospheric emissions. *Nature*, 272:682–686, April 1978. .

Thierry Dudok de Wit, Vladimir V. Krasnoselskikh, Stuart D. Bale, John W. Bonnell, Trevor A. Bowen, Christopher H. K. Chen, Clara Froment, Keith Goetz, Peter R. Harvey, Vamsee Krishna Jagarlamudi, Andrea Larosa, Robert J. MacDowall, David M. Malaspina, William H. Matthaeus, Marc Pulupa, Marco Velli, and Phyllis L. Whittlesey. Switchbacks in the Near-Sun Magnetic Field: Long Memory and Impact on the Turbulence Cascade. *Astrophys. J. Suppl.*, 246(2):39, February 2020. .

D. Forslund, R. Morse, C. Nielson, and J. Fu. Electron Cyclotron Drift Instability and Turbulence. *Phys. Fluids*, 15:1303–1318, July 1972. .

D. W. Forslund, R. L. Morse, and C. W. Nielson. Electron Cyclotron Drift Instability. *Phys. Rev. Lett.*, 25:1266–1270, November 1970. .

D. W. Forslund, R. L. Morse, and C. W. Nielson. Nonlinear Electron-Cyclotron Drift Instability and Turbulence. *Phys. Rev. Lett.*, 27:1424–1428, November 1971. .

N. J. Fox, M. C. Velli, S. D. Bale, R. Decker, A. Driesman, R. A. Howard, J. C. Kasper, J. Kinnison, M. Kusterer, and D. Lario. The Solar Probe Plus Mission: Humanity's First Visit to Our Star. *Space Science Reviews*, 204(1-4): 7–48, Dec 2016. .

S. P. Gary and J. J. Sanderson. Longitudinal waves in a perpendicular collisionless plasma shock. I. Cold ions. *J. Plasma Phys.*, 4:739, December 1970.

F. Hadi, P. H. Yoon, and A. Qamar. Ordinary mode instability associated with thermal ring distribution. *Phys. Plasmas*, 22(2):022112, February 2015. .

J. S. Halekas, P. Whittlesey, D. E. Larson, D. McGinnis, M. Maksimovic, M. Berthomier, J. C. Kasper, A. W. Case, K. E. Korreck, M. L. Stevens, K. G. Klein, S. D. Bale, R. J. MacDowall, M. P. Pulupa, D. M. Malaspina, K. Goetz, and P. R. Harvey. Electrons in the Young Solar Wind: First Results from the Parker Solar Probe. *Astrophys. J. Suppl.*, 246(2):22, February 2020a. .

J. S. Halekas, P. Whittlesey, D. E. Larson, D. McGinnis, M. Maksimovic, M. Berthomier, J. C. Kasper, A. W. Case, K. E. Korreck, M. L. Stevens, K. G. Klein, S. D. Bale, R. J. MacDowall, M. P. Pulupa, D. M. Malaspina, K. Goetz, and P. R. Harvey. Electrons in the Young Solar Wind: First Results from the Parker Solar Probe. *The Astrophysical Journal Supplement*, 246(2): 22, February 2020b. .

K. J. Harker and F. W. Crawford. Nonlinear Interaction of Cyclotron Harmonic Waves. *J. App. Phys.*, 39:5959–5968, December 1968. .

Vamsee Krishna Jagarlamudi, Olga Alexandrova, Laura Berčič, Thierry Dudok de Wit, Vladimir Krasnoselskikh, Milan Maksimovic, and Štěpán Štverák. Whistler Waves and Electron Properties in the Inner Heliosphere: Helios Observations. *The Astrophysical Journal*, 897(2):118, July 2020. .

Justin C. Kasper, Robert Abiad, Gerry Austin, Marianne Balat-Pichelin, Stuart D. Bale, John W. Belcher, Peter Berg, Henry Bergner, Matthieu Berthomier, Jay Bookbinder, Etienne Brodu, David Caldwell, Anthony W. Case, Benjamin D. G. Chand ran, Peter Cheimets, Jonathan W. Cirtain, Steven R. Cranmer, David W. Curtis, Peter Daigneau, Greg Dalton, Brahmananda Dasgupta, David DeTomaso, Millan Diaz-Aguado, Blagoje Djordjevic, Bill Donaskowski, Michael Effinger, Vladimir Florinski, Nichola Fox, Mark Freeman, Dennis Gallagher, S. Peter Gary, Tom Gauron, Richard Gates, Melvin Goldstein, Leon Golub, Dorothy A. Gordon, Reid Gurnee, Giora Guth, Jasper Halekas, Ken Hatch, Jacob Heerikuisen, George Ho, Qiang Hu, Greg Johnson, Steven P. Jordan, Kelly E. Korreck, Davin Larson, Alan J. Lazarus, Gang Li, Roberto Livi, Michael Ludlam, Milan Maksimovic, James P. McFadden, William Marchant, Bennet A. Maruca, David J. McComas, Luciana Messina, Tony Mercer, Sang Park, Andrew M. Peddie, Nikolai Pogorelov, Matthew J. Reinhart, John D. Richardson, Miles Robinson, Irene Rosen, Ruth M. Skoug, Amanda Slagle, John T. Steinberg, Michael L. Stevens, Adam Szabo, Ellen R. Taylor, Chris Tiu, Paul Turin, Marco Velli, Gary Webb, Phyllis Whittlesey, Ken Wright, S. T. Wu, and Gary Zank. Solar Wind Electrons Alphas and Protons (SWEAP) Investigation: Design of the Solar Wind and Coronal Plasma Instrument Suite for Solar Probe Plus. *Space Science Reviews*, 204(1-4):131–186, December 2016. .

A. Kumar and V. K. Tripathi. Bernstein mode coupling to cyclotron harmonic radiation in a plasma. *Phys. Plasmas*, 13:052302, May 2006. .

C. Lacombe, O. Alexandrova, L. Matteini, O. Santolík, N. Cornilleau-Wehrlin, A. Mangeney, Y. de Conchy, and M. Maksimovic. Whistler Mode Waves and the Electron Heat Flux in the Solar Wind: Cluster Observations. *The Astrophysical Journal*, 796(1):5, Nov 2014. .

W. Y. Li, D. B. Graham, Yu. V. Khotyaintsev, A. Vaivads, M. André, K. Min, K. Liu, B. B. Tang, C. Wang, K. Fujimoto, C. Norgren, S. Toledo-Redondo, P. A. Lindqvist, R. E. Ergun, R. B. Torbert, A. C. Rager, J. C. Dorelli, D. J. Gershman, B. L. Giles, B. Lavraud, F. Plaschke, W. Magnes, O. Le Contel, C. T. Russell, and J. L. Burch. Electron Bernstein waves driven by electron crescents near the electron diffusion region. *Nature Communications*, 11:141, January 2020. .

David M. Malaspina, Robert E. Ergun, Mary Bolton, Mark Kien, David Summers, Ken Stevens, Alan Yehle, Magnus Karlsson, Vaughn C. Hoxie, and Stuart D. Bale. The Digital Fields Board for the FIELDS instrument suite on the Solar Probe Plus mission: Analog and digital signal processing. *Journal of Geophysical Research (Space Physics)*, 121(6):5088–5096, Jun 2016. .

David M. Malaspina, Jasper Halekas, Laura Bercic, Davin Larson, Phyllis Whittlesey, Stuart D. Bale, John W. Bonnell, Thierry Dudok de Wit, Robert E. Ergun, Gregory Howes, Keith Goetz, Katherine Goodrich, Peter R. Harvey, Robert J. MacDowall, Marc Pulupa, Anthony W. Case, Justin C. Kasper, Kelly E. Korreck, Roberto Livi, and Michael L. Stevens. Plasma Waves near the Electron Cyclotron Frequency in the Near-Sun Solar Wind. *The Astrophysical Journal Supplement Series*, 246(2):21, February 2020. .

Michel Moncuquet, Nicole Meyer-Vernet, Karine Issautier, Marc Pulupa, J. W. Bonnell, Stuart D. Bale, Thierry Dudok de Wit, Keith Goetz, Léa Griton, Peter R. Harvey, Robert J. MacDowall, Milan Maksimovic, and David M. Malaspina. First In Situ Measurements of Electron Density and Temperature from Quasi-thermal Noise Spectroscopy with Parker Solar Probe/FIELDS. *The Astrophysical Journal Supplement Series*, 246(2):44, February 2020. .

F. S. Mozer, O. V. Agapitov, S. D. Bale, J. W. Bonnell, T. A. Bowen, and I. Vasko. DC and Low-Frequency Electric Field Measurements on the Parker Solar Probe. *Journal of Geophysical Research (Space Physics)*, 125(9):e27980, September 2020. .

M. Pulupa, S. D. Bale, J. W. Bonnell, T. A. Bowen, N. Carruth, K. Goetz, D. Gordon, P. R. Harvey, M. Maksimovic, J. C. Martínez-Oliveros, M. Moncuquet, P. Saint-Hilaire, D. Seitz, and D. Sundkvist. The Solar Probe Plus Radio Frequency Spectrometer: Measurement requirements, analog design, and digital signal processing. *Journal of Geophysical Research (Space Physics)*, 122(3): 2836–2854, March 2017. .

D. Stansby, T. S. Horbury, C. H. K. Chen, and L. Matteini. Experimental Determination of Whistler Wave Dispersion Relation in the Solar Wind. *The Astrophysical Journal: Letters*, 829(1):L16, Sep 2016. .

Yuguang Tong, Ivan Y. Vasko, Anton V. Artemyev, Stuart D. Bale, and Forrest S. Mozer. Statistical Study of Whistler Waves in the Solar Wind at 1 au. *The Astrophysical Journal*, 878(1):41, Jun 2019. .

J. L. Verniero, D. E. Larson, R. Livi, A. Rahmati, M. D. McManus, P. Sharma Pyakurel, K. G. Klein, T. A. Bowen, J. W. Bonnell, B. L. Alterman, P. L. Whittlesey, David M. Malaspina, S. D. Bale, J. C. Kasper, A. W. Case, K. Goetz, P. R. Harvey, K. E. Korreck, R. J. MacDowall, M. Pulupa, M. L. Stevens, and T. Dudok de Wit. Parker Solar Probe Observations of Proton Beams Simultaneous with Ion-scale Waves. *The Astrophysical Journal Supplement Series*, 248(1):5, May 2020. .

III Wilson, L. B., C. A. Cattell, P. J. Kellogg, K. Goetz, K. Kersten, J. C. Kasper, A. Szabo, and M. Wilber. Large-amplitude electrostatic waves observed at a supercritical interplanetary shock. *Journal of Geophysical Research (Space Physics)*, 115(A12):A12104, December 2010. .

L. B. Wilson III, L.-J. Chen, S. Wang, S. J. Schwartz, D. L. Turner, M. L. Stevens, J. C. Kasper, A. Osmane, D. Caprioli, S. D. Bale, M. P. Pulupa, C. S. Salem, and K. A. Goodrich. Electron energy partition across interplanetary shocks: II. Statistics. *Astrophys. J. Suppl.*, 245(24), December 2019. . URL https://iopscience.iop.org/article/10.3847/1538-4365/ab5445.

Y. Zhang, H. Matsumoto, and H. Kojima. Bursts of whistler mode waves in the upstream of the bow shock: Geotail observations. *Journal of Geophysical Research*, 103(A9):20529–20540, Sep 1998. .

L. L. Zhao, G. P. Zank, L. Adhikari, M. Nakanotani, D. Telloni, and F. Carbone. Spectral Features in Field-aligned Solar Wind Turbulence from Parker Solar Probe Observations. *The Astrophysical Journal*, 898(2):113, August 2020. .

Qinghua Zhou, Fuliang Xiao, Chang Yang, Si Liu, Yihua He, D. N. Baker, H. E. Spence, G. D. Reeves, and H. O. Funsten. Generation of lower and upper bands of electrostatic electron cyclotron harmonic waves in the Van Allen radiation belts. *Geophysical Research Letters*, 44(11):5251–5258, June 2017. .

Xingyu Zhu, Jiansen He, Daniel Verscharen, Die Duan, and Stuart D. Bale. Wave Composition, Propagation, and Polarization of Magnetohydrodynamic Turbulence within 0.3 au as Observed by Parker Solar Probe. *The Astrophysical Journal, Letters*, 901(1):L3, September 2020. .